*Macromolecules* **1983**, *16*, 1505–1514

lamellae oriented with their large flat faces parallel to the film surface, as well as in increase of fold period (long spacing). The increase of stress with annealing time (Figure 1) also supports the idea of an increase in entanglement mesh.

**Acknowledgment.** We are indebted to Dr. Paul Smith, Central Laboratory, DSM, Geleen, The Netherlands, for valuable discussions, comments, and suggestions. Thanks are due to Drs. R. H. Marchessault and T. Bluhm, Xerox Research Centre of Canada Ltd., Mississauga, Ontario, for their kind help in obtaining the light scattering patterns.

**Registry No.** Polyethylene, 9002-88-4.

## References and Notes

(1) M. Matsuo and R. St. J. Manley, *Macromolecules*, **15**, 985 (1982).
(2) P. Smith and P. J. Lemstra, *J. Mater. Sci.*, **15**, 505 (1980).
(3) P. Smith and P. J. Lemstra, *Makromol. Chem.*, **180**, 2983 (1979).
(4) P. Smith and P. J. Lemstra, *Colloid Polym. Sci.*, **258**, 891 (1980).
(5) P. Smith, P. J. Lemstra, and H. C. Booij, *J. Polym. Sci., Polym. Phys. Ed.*, **19**, 877 (1981).
(6) P. Smith, P. J. Lemstra, J. P. L. Pijpers, and A. M. Kiel, *Colloid Polym. Sci.*, **259**, 1070 (1981).
(7) A. Ciferri and I. M. Ward, Eds., "Ultrahigh Modulus Polymers", Applied Science Publishers, London, 1979, Chapter I.
(8) A. Keller, *J. Polym. Sci.*, **15**, 31 (1955).
(9) A. J. Pennings, J. M. A. A. van der Mark, and H. C. Booij, *Kolloid Z.-Z. Polym.*, **236**, 99 (1970).
(10) J. H. Southern and R. S. Porter, *J. Appl. Polym. Sci.*, **14**, 2305 (1970).
(11) A. Peterlin and G. Meinel, *J. Polym. Sci., Part B*, **3**, 783 (1965).
(12) M. Takayanagi, K. Imada, and T. Kajiyama, *J. Polym. Sci., Part C*, **15**, 263 (1966).
(13) W. O. Statton and P. H. Geil, *J. Appl. Polym. Sci.*, **3**, 357 (1960).
(14) M. Matsuo and R. St. J. Manley, in preparation.
(15) A. Turner-Jones, *J. Polym. Sci.*, **62**, 174, 553 (1962).
(16) P. H. Geil, *J. Polym. Sci., Part A*, **2**, 3813 (1964).
(17) M. B. Rhodes and R. S. Stein, *J. Polym. Sci., Part A-2*, **7**, 1538 (1969).
(18) M. Moritani, N, Hayashi, A. Utsuo, and H. Kawai, *Polym. J.*, **2**, 74 (1971).
(19) T. Hashimoto, Y. Murakami, N. Hayashi, and H. Kawai, *Polym. J.*, **6**, 132 (1974).
(20) T. Hashimoto, Y. Marakami, and H. Kawai, *J. Polym. Sci., Polym. Phys. Ed.*, **13**, 1613 (1975).
(21) M. Matsuo, S. Nomura, T. Hashimoto, and K. Kawai, *Polym. J.*, **6**, 151 (1974).
(22) F. Ozaki, T. Ogita, and M. Matsuo, *Macromolecules*, **14**, 299 (1981).
(23) A. J. Pennings and A. Zwijnenburg, *J. Polym. Sci., Polym. Phys. Ed.*, **17**, 1011 (1979).

---

# Ultradrawing at Room Temperature of High Molecular Weight Polyethylene. 3. Theoretical Analysis of SAXS Patterns of Unannealed and Annealed Samples

**Masaru Matsuo,[†] Masaki Tsuji, and R. St. John Manley***

*Pulp and Paper Research Institute of Canada and Department of Chemistry,*
*McGill University, Montreal, Quebec, Canada H3A 2A7. Received November 10, 1982*

ABSTRACT: Thermoreversible polyethylene gels were produced by rapidly quenching hot solutions of ultrahigh molecular weight polymer. On drying, the gel forms a film composed of large lamellar crystals stacked on top of one another to form a periodic crystalline–amorphous structure perpendicular to the plane of the film. The SAXS patterns of these dry gel films show sharp meridional maxima up to the fourth order. After the films are annealed for a short time at 110 °C, the SAXS patterns show considerable changes: viz., all the scattering maxima become broader and are displaced toward the center of the pattern, the second-order maximum becomes particularly diffuse, the third-order maximum becomes extremely weak, and the fourth-order maximum disappears completely. In order to interpret the observed changes in terms of the structure of the annealed films, the SAXS patterns were computed in terms of a two-dimensional model of periodic crystalline–amorphous structures in which there are orientational fluctuations. By analysis of the theoretical expressions and comparison with the observed intensity distribution, conclusions are drawn as to the origin and significance of the changes in the SAXS patterns on annealing.

## Introduction

It is well-known that sedimented mats of lamellar polyethylene single crystals undergo recrystallization when annealed at temperatures between 110 °C and the melting point.[1-6] The recrystallization process can be followed by small-angle X-ray scattering, which reveals that the Bragg spacings, corresponding to the diffraction maxima, increase considerably during annealing. This implies that the annealing process causes the polymer chains within the lamellae to refold into a longer fold period.

In our earlier paper[7] we reported that the small-angle X-ray scattering (SAXS) patterns from dry gel films of polyethylene, produced by gelation–crystallization from dilute solutions according to the method of Smith and Lemstra,[8-12] showed strong meridional maxima in several orders corresponding to a long period of about 10 nm. The patterns were interpreted as indicating that the dry gel films are composed of a stack of lamellar crystals that are highly oriented with their large flat faces parallel to the film surface. The SAXS patterns from these gel films are thus similar to those obtained from a sedimented mat of single crystals. When the dry gel films were stretched uniaxially at room temperature, a draw ratio of about 20 was attained and the stress remained nearly constant throughout the drawing process. On the other hand, when the dry gel film was annealed for 15 min at 110 °C, the first-order maximum became diffuse and moved closer to the center of the scattering pattern, corresponding to an increase of the fold period.[13] These changes in the SAXS

---

[†] On leave from Nara Women's University, Nara, Japan.

0024-9297/83/2216-1505$01.50/0

patterns of the dry gel films are similar to those observed in the annealing of sedimented mats of polyethylene single crystals. The maximum elongation ratio of the dry gel film annealed for 15 min was about 30, which is a considerable improvement in comparison with the maximum elongation ratio of unannealed films. The value of the stress increased with elongation ratio, and this tendency became more pronounced as the annealing time increased.

In order to understand the mechanism of the improvement in the draw ratio by annealing, it seems important to study the changes in the SAXS patterns in detail. Accordingly, the present paper is concerned with a quantitative evaluation of the changes in the SAXS patterns caused by annealing. The scattering is attributed to an alternation in texture between crystalline and amorphous intercrystalline regions, in which both regions fluctuate in thickness about their respective mean values. Crist[19] has reviewed existing one-dimensional models for calculating the SAXS of semicrystalline polymers; his discussion is mainly concerned with the effect of the type of distribution function, describing the lamellar thickness fluctuations, on the scattering maxima. According to Tsvankin[18] and Blundel,[14,15] the scattering phenomenon is considered in terms of a one-dimensional model in which a transition zone is introduced between each phase, so that there is a linear change in density from the crystalline to the amorphous value. In the theory, the scattering was assumed to be caused by the excess electron density. However, in such a one-dimensional model, a more realistic mathematical treatment can be made on the basis of the concept that the scattering is caused by positive and negative deviations from the average density of the sample.[17] In the present paper we propose a two-dimensional model in order to derive an expression for the distribution of intensity in the SAXS pattern for a system of stacked folded-chain lamellae in which there are orientation fluctuations. In such a system, it is too complicated to represent the scattered intensity by introducing the average density. Therefore we followed Blundell's concept that the scattering is due to the excess electron density. Then by analysis of the theoretical expressions and comparison with the observed intensity distribution, conclusions are drawn as to the origin of the changes in the SAXS patterns on annealing.

## Experimental Section

The polymer used was a linear polyethylene with a molecular weight of $6 \times 10^6$ (Hercules 1900/90209). Solutions containing 0.5 wt % of the polymer in Decalin were prepared as described earlier.[7] The hot solutions were poured into an aluminum tray surrounded by ice water to form a gel. The Decalin was allowed to evaporate from the gel at ambient temperature for about 14 days. The nearly dried film was immersed in an excess of ethanol for 1 day in order to remove residual traces of Decalin. Finally the film was dried in a vacuum oven and cut into strips.

The samples were annealed in a silicone oil bath at 110 °C for 45 s. This temperature has been reported to be the lowest temperature where an increase of the long period in polyethylene single crystal mats is observed on annealing. The SAXS patterns of the original and annealed samples were photographically recorded under vacuum, with the X-ray beam directed parallel to the film surface, using nickel-filtered Cu K$\alpha$ radiation (40 kV, 35 mA) and circular pinhole collimation. The meridional intensity distribution of the observed SAXS patterns was obtained from microdensitometer (Joyce-Loebl MK III CS) tracings as an optical density distribution.

## Results and Discussion

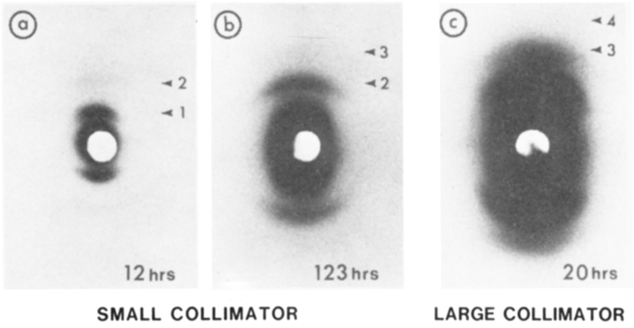

**Figure 1.** Change in the SAXS pattern of an unannealed film with increasing X-ray exposure. The numbers indicate the order of the reflections.

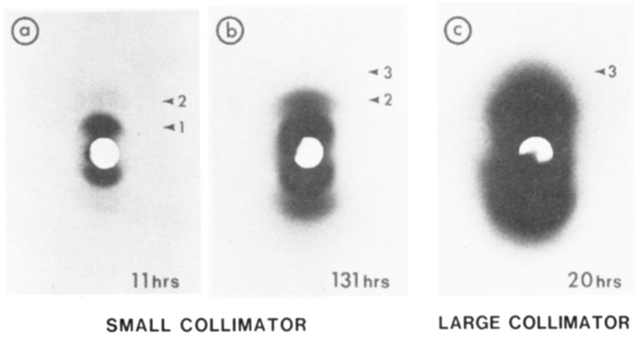

**Figure 2.** Change in the SAXS pattern of a film annealed at 110 °C for 45 s with increasing X-ray exposure. The numbers indicate the order of the reflections.

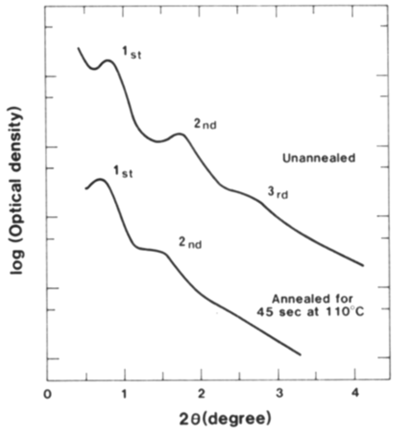

**Figure 3.** Two SAXS intensity distributions as a function of twice the Bragg angle ($2\theta$) in the meridional direction, which were obtained as an optical density distribution from the X-ray films with the small collimator. No correction for instrumental broadening has been introduced.

**SAXS Observations.** Figure 1 shows the change in the SAXS pattern of the unannealed sample with increasing X-ray exposure. In appropriate exposures the scattering maxima in the meridional direction appeared up to the fourth order (see Figure 1c). This indicates that the specimens are composed of lamellar crystals that are highly oriented with their large flat faces parallel to the film surface. Furthermore, the identity period and lamellar thickness can be assumed to be essentially constant.

Figure 2 shows the scattering pattern of a specimen annealed for 45 s. Although the annealing time was short, the scattering pattern shows considerable changes: all the scattering maxima become broader and are displaced toward the center of the pattern, the second-order maximum becomes particularly diffuse, the third-order maximum becomes extremely weak, and the fourth-order maximum disappears completely. These changes are also seen in Figure 3, which shows the optical density distribution in the meridional direction as obtained from microdensitometer tracings of the photographic SAXS patterns. The

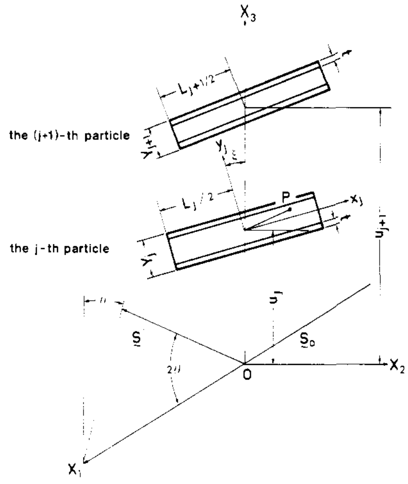

**Figure 4.** Model used for the theoretical analysis of the SAXS intensity distribution.

maxima are rather broad because corrections for instrumental broadening have not been introduced. It should be noted that the intensity distributions in Figure 3 were obtained as a single master curve by applying arbitrary scaling factors so as to superimpose the densitometer tracings corresponding to the different exposure times. These observations indicate that the lamellar crystals undergo large changes in their orientation, thickness, and identity period as a result of the recrystallization associated with the refolding to a longer fold period.

## Theoretical Analysis

The changes in the SAXS intensity distribution of the dry gel film induced by the annealing process can be analyzed quantitatively in terms of a model having two-dimensional electron density fluctuations similar to that of Blundell.[14,15] Figure 4 shows a schematic diagram illustrating the model used for the theoretical analysis of the experimentally observed scattered intensity distribution. The axes $X_1$ and $X_3$ are respectively parallel to the direction of the incident X-ray beam, whose unit vector is defined as $\mathbf{s}_0$, and parallel to the direction normal to the film surface. The sample is thus oriented edgewise to the X-ray beam. The SAXS pattern is observed as a function of twice the Bragg angle ($2\theta$) and the azimuthal angle $\mu$, where $\mathbf{s}'$ is a unit vector along the scattered X-ray beam. In order to simplify the calculations it is assumed that the crystal lamellae are rectangular in cross section and situated in the plane O–$X_3$–$X_2$, so that the center of gravity of each lamella lies on the $X_3$ axis. The dimensions of the $j$th particle are represented by the length $L_j$ and the thickness $Y_j$. The coordinate system O–$x_jy_jz_j$ is fixed within the $j$th lamella and $\xi$ denotes the orientational angle between the $y_j$ and $X_3$ axes.

According to the results in the earlier work,[7,13] the polymer chains are arranged approximately perpendicular to the plane of the lamellae and the chains fold back upon themselves on reaching the planar surface of the lamellae. The presence of the chain folds implies that there is a fluctuation of the electron density within the lamellae, and presumably the extent of the fluctuation reaches a maximum at the boundary surface. The lamellae are assumed to stack together to give a periodic one-dimensional crystal–amorphous structure arranged at right angles to the plane of the lamellae. Following Blundell, this crystalline–amorphous structure is represented by a model in which the density between the crystalline and amorphous phases changes linearly over a finite transition range, such that the electron density profile has the shape of a repeated trapezium as shown in Figure 5. The lengths $Y_j$ and $Z_j$ are those of the respective phases, and $X_j$ is the total length of the $j$th pair of crystalline–amorphous phases. The length $t$ denotes the dimension of the transition region. If the value of $t$ is very small in comparison with that of $Y_j$, most of the folds are sharp and regular.

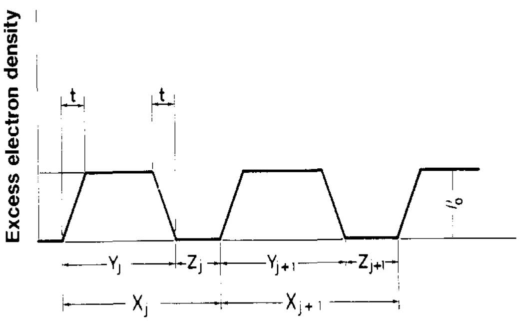

**Figure 5.** Trapezoidal model for the electron density variation between the crystalline and amorphous phases.

The model in Figure 5 can be applied exactly in the case where the angle $\xi$ in Figure 4 is set at zero. In this case the abscissa in Figure 5 is coincident with the $X_3$ axis and the ordinate shows the excess electron density $\rho_0 = \rho_c - \rho_a$, $\rho_c$ and $\rho_a$ being the electron densities of the crystalline and amorphous phases, respectively. In order to avoid difficulties in the mathematical procedure, it is assumed that the trapezoidal model for the electron density variation is approximately valid when the degree of orientational fluctuation of the lamellae is small. Such a one-dimensional trapezoidal model was first proposed by Tsvankin.[18]

For the calculations let the unit vectors along $X_3$, $X_2$, $X_1$, $y_j$, and $x_j$ be $\mathbf{k}$, $\mathbf{j}$, $\mathbf{i}$, $\mathbf{j}'$, and $\mathbf{i}'$, respectively. Considering the geometrical arrangement of the lamellae in Figure 4, the scattering amplitude from the $j$th lamella whose center of gravity is situated at a distance $u_j$ from the center of the coordinate system O–$X_1X_2X_3$ is given by

$$a_j(\mathbf{s}) = \int_s \rho(\mathbf{r}_j) \exp[-2\pi i(\mathbf{s}\cdot\mathbf{r}_j)]\,\mathrm{d}S = \int_s \rho(\mathbf{r}_j) \exp[-2\pi i \mathbf{s}(u_j\mathbf{k} + x_j\mathbf{i}' + y_j\mathbf{j}')]\,\mathrm{d}S \quad (1)$$

where $\rho(\mathbf{r}_j)$ is the electron density at point P within the $j$th particle and $\mathbf{s} = (\mathbf{s}' - \mathbf{s}_0)/\lambda$. If we choose $\rho_a$ as a reference base, $\rho(\mathbf{r}_j)$ corresponds to $\rho_c(\mathbf{r}_j) - \rho_a$.

From the boundary conditions of $\rho(\mathbf{r}_j)$ in Figure 4, $\rho(\mathbf{r}_j)$ is given by

$$\begin{aligned}
\rho(\mathbf{r}_j) &= \frac{\rho_0}{t}\cdot\left(\frac{Y_j}{2} + y_j\right), && \begin{cases} -\dfrac{Y_j}{2} \leqq y_j \leqq -\dfrac{Y_j}{2} + t \\ -L_j/2 \leqq x_j \leqq L_j/2 \end{cases} \\
&= \rho_0, && \begin{cases} -\dfrac{Y_j}{2} + t \leqq y_j \leqq \dfrac{Y_j}{2} - t \\ -L_j/2 \leqq x_j \leqq L_j/2 \end{cases} \qquad (2) \\
&= \frac{\rho_0}{t}\left(\frac{Y_j}{2} - y_j\right), && \begin{cases} \dfrac{Y_j}{2} - t \leqq y_j \leqq \dfrac{Y_j}{2} \\ -L_j/2 \leqq x_j \leqq L_j/2 \end{cases}
\end{aligned}$$

Substituting eq 2 into eq 1 allows us to rewrite $a_j(\mathbf{s})$ as follows:

$$a_j(\mathbf{s}) = \rho_0 \frac{\sin(\pi A_j L_j)}{\pi A_j} \frac{[\cos\{\pi B_j(Y_j - 2t)\} - \cos(\pi B_j Y_j)]}{2t(\pi B_j)^2} \times \exp[-2\pi i u_j(\mathbf{s}\cdot\mathbf{k})] \quad (3a)$$

$$= f_j \exp[-2\pi i b u_j] \quad (3b)$$

where

$$b = s \cos \mu \tag{4a}$$

$$s = (1/\lambda) \sin 2\theta \tag{4b}$$

$$A_j = (1/\lambda) \sin 2\theta \sin (\mu + \xi) \tag{4c}$$

$$B_j = (1/\lambda) \sin 2\theta \cos (\mu + \xi) \tag{4d}$$

and

$$f_j = \rho_0 \frac{\sin (\pi A_j L_j)}{\pi A_j} \frac{[\cos \{\pi B_j (Y_j - 2t)\} - \cos (\pi B_j Y_j)]}{2t(\pi B_j)^2} \tag{4e}$$

According to the method proposed by Blundell,[14] the normalized scattering intensity from an assembly of $N$ lamellae is $\sum_i \sum_j a_j(\mathbf{s}) a_i^*(\mathbf{s}) / N\bar{X}$. $a^*(\mathbf{s})$ denotes the complex conjugate of $a(\mathbf{s})$, and $\bar{X}$ denotes the mean periodic distance. As the result

$$I = \frac{1}{N\bar{X}} \sum_{i=1}^{N} \sum_{j=1}^{N} a_j(\mathbf{s}) a_i^*(\mathbf{s}) = I_B - I_C \tag{5}$$

where $I_B$ and $I_C$ are given by

$$I_B = \mathrm{Re} \left[ \frac{1}{\bar{X}} \left\{ J + \frac{2 G_y^2 F_x}{1 - F_x} \right\} \right] = \mathrm{Re} \left[ \frac{1}{\bar{X}} \left\{ J - G_y^2 + \frac{1 + F_x}{1 - F_x} G_y^2 \right\} \right] \tag{6}$$

and

$$I_C = \mathrm{Re} \left[ \frac{G_y^2}{N\bar{X}} \left\{ \frac{2F_x (1 - F_x^N)}{(1 - F_x)^2} \right\} \right] \tag{7}$$

and where

$$J = \int_0^{2\pi} \int_{-\infty}^{\infty} \int_{-\infty}^{\infty} p(\xi) M(Y_j) h(L_j) f_j^2 \, \mathrm{d}Y_j \, \mathrm{d}L_j \, \mathrm{d}\xi \Big/ \int_0^{2\pi} p(\xi) \, \mathrm{d}\xi \tag{8a}$$

$$G_y = \int_0^{2\pi} \int_{-\infty}^{\infty} \int_{-\infty}^{\infty} p(\xi) M(Y_j) h(L_j) f_j \, \mathrm{d}Y_j \, \mathrm{d}L_j \, \mathrm{d}\xi \Big/ \int_0^{2\pi} p(\xi) \, \mathrm{d}\xi \tag{8b}$$

and

$$F_x = \int_{-\infty}^{\infty} H(X_j) \exp(-2\pi i b X_j) \, \mathrm{d}X_j \tag{8c}$$

Following Blundell,[14,15] we assume that the variations of the lengths $Y_j$, $X_j$, and $L_j$ are independent and are given by the following symmetric Gaussian functions with the respective mean lengths of $\bar{Y}$, $\bar{X}$, and $\bar{L}$ and the standard deviations $\sigma_y$, $\sigma_x$, and $\sigma_l$; thus

$$h(L_j) = (2\pi)^{-1/2} \sigma_l^{-1} \exp[-(L_j - \bar{L})^2 / 2\sigma_l^2] \tag{9a}$$

$$M(Y_j) = (2\pi)^{-1/2} \sigma_y^{-1} \exp[-(Y_j - \bar{Y})^2 / 2\sigma_y^2] \tag{9b}$$

and

$$H(X_j) = (2\pi)^{-1/2} \sigma_x^{-1} \exp[-(X_j - \bar{X})^2 / 2\sigma_x^2] \tag{9c}$$

Substituting eq 9a–c into eq 8a–c, we obtain

$$J = \frac{\bar{L}^2 \bar{Y}^2 \rho_0^2}{4} \int_0^{2\pi} p(\xi) \frac{\sin^2 (\pi B_j t)}{(\pi A_j \bar{L})^2 (\pi B_j \bar{Y})^2 (\pi B_j t)^2} \times \{1 - \cos (2\pi A_j \bar{L}) \exp(-2\pi^2 A_j^2 \sigma_l^2)\} \times \{1 - \cos (2\pi B_j \bar{Y} - 2\pi B_j t) \exp(-2\pi^2 B_j^2 \sigma_y^2)\} \, \mathrm{d}\xi \Big/ \int_0^{2\pi} p(\xi) \, \mathrm{d}\xi \tag{10a}$$

$$G_y = \bar{L} \bar{Y} \rho_0 \int_0^{2\pi} p(\xi) \frac{\sin (\pi A_j \bar{L})}{\pi A_j \bar{L}} \exp\left\{-\frac{1}{2} \pi^2 A_j^2 \sigma_l^2\right\} \times \frac{\sin (\pi B_j \bar{Y} - \pi B_j t)}{\pi B_j \bar{Y}} \frac{\sin (\pi B_j t)}{\pi B_j t} \exp\left\{-\frac{1}{2} \pi^2 B_j^2 \sigma_y^2\right\} \mathrm{d}\xi \Big/ \int_0^{2\pi} p(\xi) \, \mathrm{d}\xi \tag{10b}$$

and

$$F_x = \exp\{-2\pi i b \bar{X}\} |F| \tag{11a}$$

where

$$|F| = \exp\{-2\pi^2 b^2 \sigma_x^2\} \tag{11b}$$

In eq 5 the term $I_B$ is associated with the first and higher order scattering maxima, and the term $I_C$ is associated with zero-order scattering. The term $J - G_y^2$ in eq 6 corresponds to diffuse scattering, and its value becomes zero if all fluctuations concerning $\sigma_l$, $\sigma_y$, and $p(\xi)$ are zero. The term $\mathrm{Re}\,\{(1 + F_x)/(1 - F_x)\}$ is a so-called reciprocal lattice factor. By using eq 11a,b, we rewrite the lattice factor as follows:

$$\mathrm{Re} \left\{ \frac{1 + F_x}{1 - F_x} \right\} = \frac{1 - |F|^2}{1 + |F|^2 - 2|F| \cos (2\pi b \bar{X})} \tag{12}$$

It is well-known that at $\mu = 0°$ eq 12 has very large values when $s\bar{X}$ is an integer and very small values when $s\bar{X}$ is not an integer. Blundell has proposed that $I_C$ can be neglected if $N$ is sufficiently large and/or if the distribution functions $H(X_j)$, $h(L_j)$, and $M(Y_j)$ are sufficiently broad. In the present case these conditions do not apply and therefore it is necessary to estimate the contribution of $I_C$ to the scattered intensity. In order to do so we calculate the term $\mathrm{Re}\,\{F_x(1 - F_x^N)/N(1 - F_x)^2\}$ in eq 7. Thus

$$\mathrm{Re} \left\{ \frac{F_x (1 - F_x^N)}{N(1 - F_x)^2} \right\} = \frac{I_{C1} + I_{C2}}{N\{1 - 2|F| \cos (2\pi s \bar{X} \cos \mu) + |F|^2\}^2} \tag{13}$$

where

$$I_{C1} = |F| \{(1 + |F|^2) \cos (2\pi s \bar{X} \cos \mu) - 2|F|\} \tag{14}$$

and

$$I_{C2} = \{-|F|^N \cos [2\pi (N + 1) s \bar{X} \cos \mu] + 2|F|^{N+1} \cos [2\pi N s \bar{X} \cos \mu] - |F|^{N+2} \cos [2\pi (N - 1) s \bar{X} \cos \mu]\} |F| \tag{15}$$

From eq 15 it is evident that the $I_{C2}$ term is an oscillating function with a much smaller period than the denominator of eq 13. Consequently, $\mathrm{Re}\,\{F_x(1 - F_x^N)/N(1 - F_x)^2\}$ has subsidiary maxima. Then the calculated intensity $I$ of eq 5 must also have subsidiary maxima due to the $I_{C2}$ term. This tendency is particularly marked for the meridional scattering ($\mu = 0$). Hashimoto et al.[16] have demonstrated that these maxima appear in the theoretical meridional scattering curve at small angles $s\bar{X} < 3$ when it is assumed that the system contains a constant discrete number ($N$) of lamellae. But in a real system the portion of the specimen sampled by the X-ray beam contains a distri-

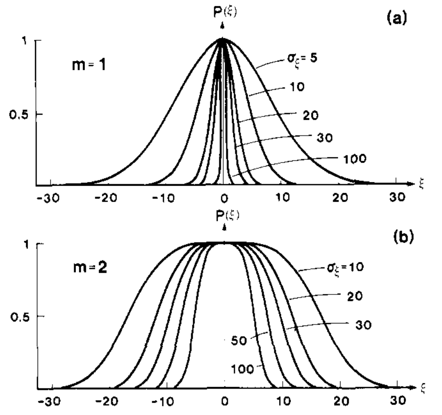

**Figure 6.** Change in the profile of the orientation distribution function of lamellae specified by $p(\xi)$ with two adjustable parameters $\sigma_\xi$ and $m$ ($\xi$ in degrees).

bution of $N$. This concept must be introduced in order to smear out the many subsidiary maxima that appear at lower scattering angles $s\bar{X}$. This has been taken into consideration by Hashimoto et al.[16] by introducing a discrete symmetrical distribution of $N$ with standard deviation $\sigma_N = 3$. This distribution is written as

$$P(N) = \exp\left\{-\frac{(N-\bar{N})^2}{2\sigma_N^{\,2}}\right\} \bigg/ \sum_{N=1}^{2\bar{N}-1} \exp\left\{-\frac{(N-\bar{N})^2}{2\sigma_N^{\,2}}\right\} \quad (16)$$

In the present work we will assume the same type of distribution of $N$. Then the average value of the term $I_C$ is given by

$$\langle I_C \rangle = \sum_{N=1}^{2\bar{N}-1} I_C P(N) \quad (17)$$

In our subsequent calculations we assume an average $\bar{N}$ of 10.

To complete this theoretical analysis we now discuss the function $p(\xi)$ that appears in eq 8. $p(\xi)$ is a distribution function describing the orientation of the lamellae with respect to the $X_3$ axis. It is defined by

$$p(\xi) = \exp[-\sigma_\xi^{\,2} \sin^{2m} \xi] \quad (18)$$

where $\sigma_\xi$ and $m$ are parameters associated with the shape of $p(\xi)$. In order to avoid the overlap of neighboring lamellae, the values of these two parameters must be chosen carefully.

Figure 6 shows the change in the profile of $p(\xi)$ with various values of $\sigma_\xi$ and $m$. $p = \bar{Y}/\bar{L}$, $q = \bar{X}/\bar{L}$, and $\chi = (\bar{Y} - t)/\bar{X}$ are fixed as 0.4, 0.727, and 0.55, respectively, in the case of $t = 0$. In the case of $\sigma_\xi = 100$ and $m = 1$, $p(\xi)$ shows a sharp distribution, and most of the lamellae orient perpendicular to the $X_3$ axis. When $\sigma_\xi = 20$ and $m = 2$, $p(\xi)$ shows a broad distribution with maximum fluctuation, and under these conditions overlapping of neighboring lamellae is avoided. In most of our subsequent calculations we will make use of these two pairs of parameters that characterize two extremes of the distribution $p(\xi)$, the one narrow and the other broad.

## Comparison of Experimental and Calculated Results

According to the theoretical analysis, the scattered intensity depends upon the structural parameters $\chi$, $\sigma_x$, $\sigma_y$, $\sigma_l$, $t$, $\sigma_\xi$, and $m$. Before carrying out the numerical calculations to evaluate the scattered intensity, we note that since $(\bar{L}\bar{Y}\rho_0)^2/\bar{X}$ depends on the absolute intensity but not on the shape of the intensity distribution function, the intensity in eq 5 was normalized by dividing by $(\bar{L}\bar{Y}\rho_0)^2/\bar{X}$. By so doing, the values of $G_y^{\,2}$ and $J$ at $s\bar{X} = 0$ are close to unity and the value of $I$ at $s\bar{X} = 0$ is close to 10.

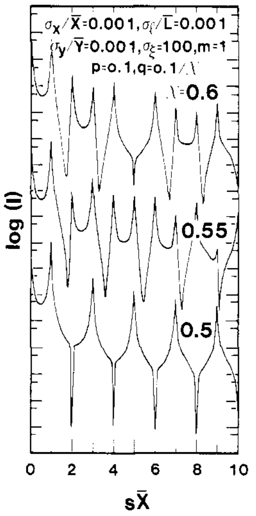

**Figure 7.** Effect of volume crystallinity, $\chi$, on the meridional scattering curves.

Consider first the effect of the crystallinity $\chi$ on the meridional scattering intensity curves. Measurements of $\chi$ by the specific volume method gave values that lay in the range 50–60%. A precise value could not be obtained, probably because of voids in the samples. Therefore in carrying out the calculations, we assume that $\chi$ has values of 0.5, 0.55, and 0.6; the parameters describing the fluctuation in the dimensions of the lamellae were set at very small values such as $\sigma_y/\bar{Y} = \sigma_l/\bar{L} = \sigma_x/\bar{X} = 0.001$ and, for the sake of simplicity, the lamellae were assumed to be oriented perpendicular to the direction of the $X_3$ axis by adopting $\sigma_\xi = 100$ and $m = 1$. In this case the overlapping of neighboring lamellae can be avoided for $p = 0.1$ and $q = 0.1/\chi$.

As illustrated in Figure 7 the curve for $\chi = 0.55$ exhibits maxima up to the eighth order but the ninth order is missing. In the curve for $\chi = 0.6$ the maximum at $s\bar{X} = 5$ is missing, and when $\chi = 0.5$ the curve exhibits maxima only at $s\bar{X} = 2n - 1$ and minima at $s\bar{X} = 2n$ ($n$ integer). This $\chi$ dependence of the curves of scattered intensity arises from the square of the "averaged structure factor", $G_y^{\,2}$. This can readily be demonstrated as follows. When $t = 0$, $\chi = \bar{Y}/\bar{X}$ and from eq 10b, $G_y^{\,2}$ can be rewritten as follows with $\xi = 0$ and $\mu = 0$:

$$G_y^{\,2} = \left[\bar{L}\bar{Y}\rho_0 \frac{\sin(\pi\chi s\bar{X})}{\pi\chi s\bar{X}} \exp\left\{-\frac{1}{2}(\pi s\bar{X})^2(\sigma_y/\bar{Y})^2\chi^2\right\}\right]^2 \quad (19)$$

In eq 19, when $\chi = 0.5$, the term $\sin(\pi\chi s\bar{X})/(\pi\chi s\bar{X})$ becomes zero at $s\bar{X} = 2n$ ($n$ = integer). Similarly, when $\chi = 0.55$ and 0.6, $G_y^{\,2}$ is equal to zero around $s\bar{X} = 9$ and 5, respectively. Thus it can be seen that when $\chi = 0.5$, 0.55, and 0.6, the behavior of $G_y^{\,2}$ is similar to that of the scattered intensity $I$, and only $\chi = 0.55$ gives scattering maxima up to high orders. Accordingly, in what follows, $\chi = 0.55$ has been adopted in order to analyze the effect of the various structure parameters on the distribution of scattered intensity.

Figures 8 and 9 show the effect of $p(\xi)$, the orientation distribution of crystal lamellae as defined by eq 18, on the meridional scattered intensity $I$ and the functions $I_B$, $G_y^{\,2}$, and $J - G_y^{\,2}$. As seen in Figures 8c and 9c, the profile of $G_y^{\,2}$ shows many maxima whose magnitudes decrease with increasing $s\bar{X}$. The decrease in the magnitude of $G_y^{\,2}$ with

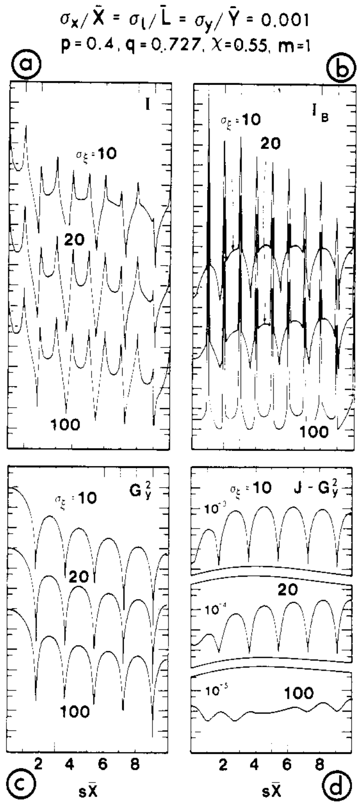

**Figure 8.** Effect of orientation distribution of lamellae, $p(\xi)$, on the meridional scattering curves in the case of $m = 1$.

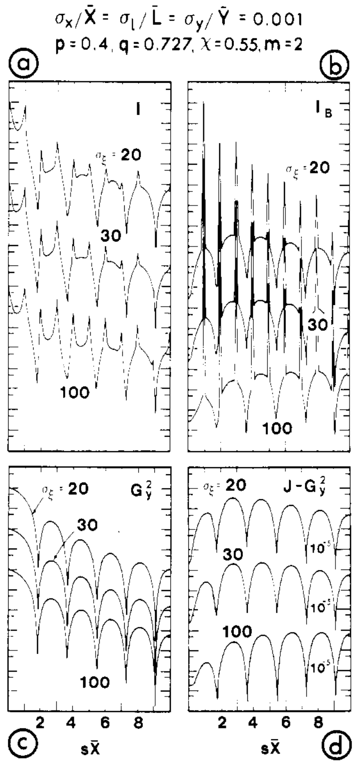

**Figure 9.** Effect of orientation distribution of lamellae, $p(\xi)$, on the meridional scattering curves in the case of $m = 2$.

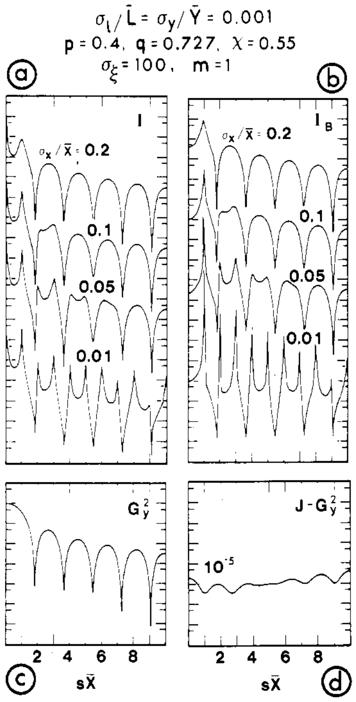

**Figure 10.** Effect of the degree of fluctuation of long period, $\sigma_x$, on the meridional scattering curves. $p(\xi)$ is given by $\sigma_\xi = 100$ and $m = 1$.

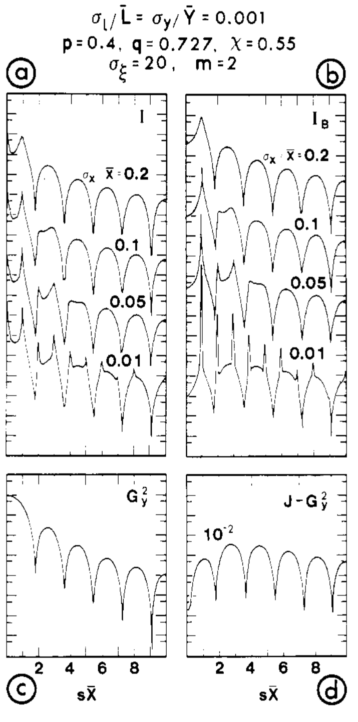

**Figure 11.** Effect of the degree of fluctuation of long period, $\sigma_x$, on the meridional scattering curves. $p(\xi)$ is given by $\sigma_\xi = 20$ and $m = 2$.

$s\bar{X}$ is somewhat pronounced when the orientation fluctuation is increased (i.e., $\sigma_\xi$ decreases). However, $G_y^2$ is not greatly affected by the orientation fluctuation of lamellae. Figures 8d and 9d show the profile of $J - G_y^2$ for various values of the orientation fluctuation parameter $\sigma_\xi$. When $m = 1$, with increasing $\sigma_\xi$ the magnitude of $J - G_y^2$ decreases and the shape of the profile changes. When $m = 2$, the magnitude and the profile of the $J - G_y^2$ curves are hardly affected by the increase of $\sigma_\xi$. This result indicates that the magnitude and the shape of $J - G_y^2$ are strongly affected when the orientation fluctuation of the lamellae is not so large (i.e., $m = 1$) but are hardly affected when the orientation fluctuation is somewhat greater (i.e., $m = 2$).

The profile of $J - G_y^2$ is reflected in the background of the profile of $I_B$. The intensity of $I_B$ at $s\bar{X} = n$ ($n$ = integer) is principally determined by the lattice factor (eq 12), and therefore the profile of $I_B$ consists of intense sharp

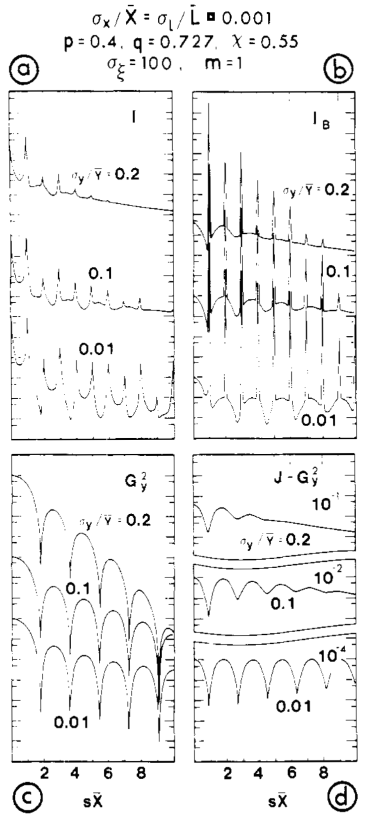

**Figure 12.** Effect of the degree of fluctuation of the lamellar thickness, $\sigma_y$, on the meridional scattering curves. $p(\xi)$ is given by $\sigma_\xi = 100$ and $m = 1$.

peaks, superimposed on the background defined by $J - G_y^2$. The peak intensity of $I_B$ decreases with increasing $s\bar{X}$. This is due to the characteristic behavior of the function $G_y^2$, which exhibits damped behavior with increasing $s\bar{X}$. The peaks of $I$ at $s\bar{X} = n$ ($n$ = integer) are broader than those of $I_B$. This is due to the addition of the $I_C$ term, which denotes the zero-order scattering. Thus the $I_C$ term is presumably a smooth curve showing broader maxima at $s\bar{X} = n$ ($n$ = integer).

Figures 10 and 11 show the effect of $\sigma_x/\bar{X}$ (the fluctuation of the identity period) on $I$, $I_B$, $G_y^2$, and $J - G_y^2$. The sets of parameters used in the calculations are $\sigma_\xi = 100$ and $m = 1$ for Figure 10 and $\sigma_\xi = 20$ and $m = 2$ for Figure 11. $G_y^2$ and $J - G_y^2$ are not affected by changes in $\sigma_x/\bar{X}$. The peak profiles of $I_B$ in Figures 10 and 11 are broader than those in Figures 8 and 9. For $\sigma_x/\bar{X} \geq 0.1$, the profiles of $I_B$ in Figures 10 and 11 are of similar shape and they are independent of the orientation fluctuation as defined by $p(\xi)$. Furthermore, the profile of $I_B$ at $s\bar{X} > 4$ is similar to that of $G_y^2$, which is independent of $\sigma_x/\bar{X}$. This is due to the characteristic behavior of the reciprocal lattice factor Re $\{(1 + F_x)/(1 - F_x)\}$, which exhibits broader peaks at $s\bar{X} = n$ ($n$ = integer) and converges rapidly to unity as $s\bar{X}$ increases for larger $\sigma_x/\bar{X}$. Finally, it is seen that the intensity distribution of $I_B$ closely resembles that of $I$ except for the region $0 < s\bar{X} \leq 1$ at $\sigma_x/\bar{X} \geq 0.1$. This is a characteristic of $I_C$ as defined by eq 7, which approaches zero when $\sigma_x/\bar{X}$ increases (see also eq 13–15 and 11b).

Figures 12 and 13 show the effect of $\sigma_y/\bar{Y}$ (fluctuation of the lamellar thickness) on $I$, $I_B$, $G_y^2$, and $J - G_y^2$. The parameters for the lamellar orientation used in the calculation are $\sigma_\xi = 100$ and $m = 1$ for Figure 12 and $\sigma_\xi = 20$ and $m = 2$ for Figure 13. The profile of $G_y^2$ shows many maxima whose magnitudes decrease rapidly at larger values of $s\bar{X}$ as $\sigma_y/\bar{Y}$ increases. The profiles in Figures 12c and 13c are hardly affected by fluctuations in the lamellar orientation $p(\xi)$. On the other hand, the magnitude of $J - G_y^2$ depends on the orientation fluctuation of lamellae $p(\xi)$. The magnitude at $m = 1$ and $\sigma_\xi = 100$ (i.e., small fluctuation) in Figure 12d increases as $\sigma_y/\bar{Y}$ increases, while that at $m = 2$ and $\sigma_\xi = 20$ (i.e., large fluctuation) in Figure 13d is hardly affected by $\sigma_y/\bar{Y}$. Furthermore, the many maxima that appear in the profile of $J - G_y^2$ when $\sigma_y/\bar{Y} = 0.01$ disappear at higher values of $s\bar{X}$ as $\sigma_y/\bar{Y}$ increases. This tendency is more marked when $m = 2$ and $\sigma_\xi = 20$. The height of the intensity maxima of $I_B$ decreases considerably at larger values of $s\bar{X}$ with increasing $\sigma_y/\bar{Y}$. This depends on the considerable decrease of peak intensities of $G_y^2$ as shown in Figures 12b and 13b. For $\sigma_y/\bar{Y} = 0.2$, the background of $I_B$ at $s\bar{X} \geq 4$ shows a monotonically decreasing line due to $J - G_y^2$, but for $\sigma_y/\bar{Y} = 0.01$ the background shows many maxima. Thus the background of $I_B$ does not reflect the profile of $G_y^2$ but of $J - G_y^2$, as far as the set of parameters listed in Figures 12 and 13 is concerned. This result suggests that the increase of $\sigma_y/\bar{Y}$ causes the smooth background of $I_B$ while the increase of $\sigma_x/\bar{X}$, as discussed in Figures 10 and 11, makes the peaks of $I_B$ broader and gives a similar profile to $G_y^2$. It is important to note that in the profile of $I$ (Figures 12a and 13a) the peak intensities are lower than those of $I_B$. This is due to the addition of the $I_C$ term, which makes the peak intensity of $I$ weak.

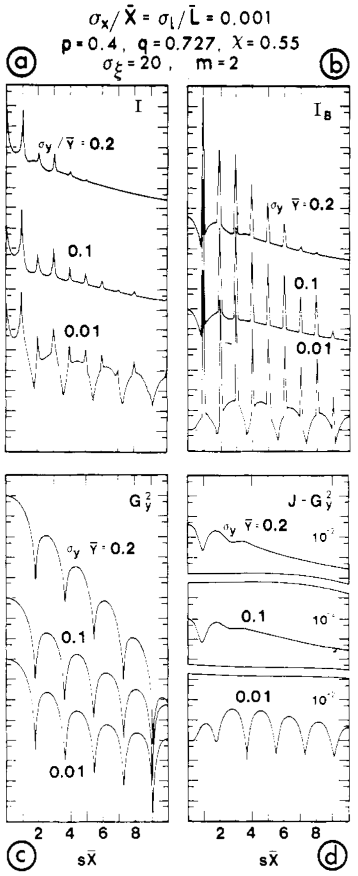

**Figure 13.** Effect of the degree of fluctuation of the lamellar thickness, $\sigma_y$, on the meridional scattering curves. $p(\xi)$ is given by $\sigma_\xi = 20$ and $m = 2$.

From a series of curves calculated for the various parameters as shown in Figures 7–13, it is concluded that the distribution of scattered intensity is most sensitive to the two parameters $\sigma_y/\bar{Y}$ and $\sigma_x/\bar{X}$. An increase of $\sigma_y/\bar{Y}$ gives rise to curves of scattered intensity ($I$) with a smooth background, while on the other hand, an increase of $\sigma_x/\bar{X}$ causes the peaks of the scattering curve to broaden. Accordingly, these two parameters were estimated by trial

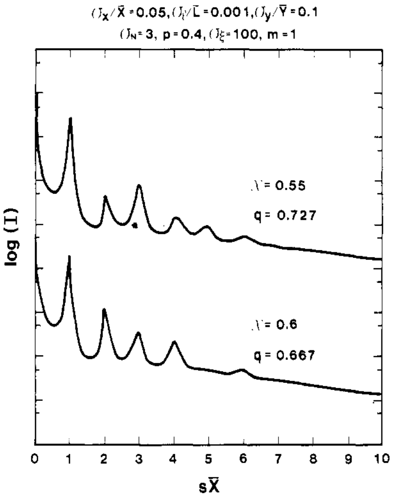

**Figure 14.** Meridional scattering curves for $\chi = 0.55$ and 0.6 in which $\sigma_y/\bar{Y} = 0.1$ and $p(\xi)$ is given by $\sigma_\xi = 100$ and $m = 1$.

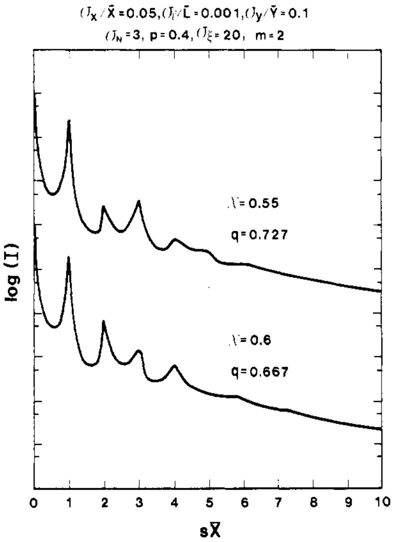

**Figure 15.** Meridional scattering curves for $\chi = 0.55$ and 0.6 in which $\sigma_y/\bar{Y} = 0.1$ and $p(\xi)$ is given by $\sigma_\xi = 20$ and $m = 2$.

and error so as to obtain the best fit between the observed and calculated curves of scattered intensity.

Figures 14 and 15 show the curves for the meridional scattered intensity $I$ as calculated for $\sigma_y/\bar{Y} = 0.1$ and $\sigma_x/\bar{X} = 0.05$. The curves in Figure 14 (calculated with $m = 1$ and $\sigma_\xi = 100$) are for the case where the lamellae orient almost parallel to the direction of the $X_3$ axis, while those in Figure 15 (calculated with $m = 2$ and $\sigma_\xi = 20$) are for the case where the lamellae have a large orientational fluctuation. It is evident that the difference in the orientational fluctuation causes no significant change in the profile.

As illustrated in Figures 14 and 15, the curves calculated for $\chi = 0.55$ show that the intensity of the second-order peak is weaker than that of the third-order peak. By contrast, for $\chi = 0.6$ the intensity of the second-order peak is stronger than that of the third-order peak. This latter tendency is in good agreement with the observed scattering curves (Figure 3). In particular, the calculated profiles for $\chi = 0.6$ are in good agreement with the curve observed for the unannealed sample when the instrumental broadening is taken into account. It should be noted that the curves for $\chi = 0.6$ in Figures 14 and 15 do not show a trough around $s\bar{X} = 5$ and in this sense, they differ from the profile shown in Figure 7. The difference is due to the large value of the parameter $\sigma_y/\bar{Y}$ (=0.1) used in Figures 14 and 15; this has the effect of giving a smooth monotonically decreasing line of $J - G_y^2$, as discussed previously for Figures 12 and 13.

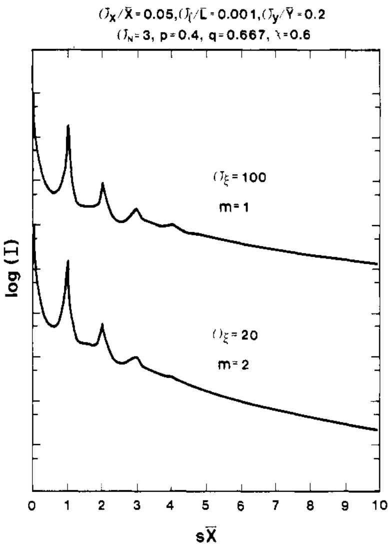

**Figure 16.** Meridional scattering curves for $\sigma_\xi = 100$, $m = 1$ and $\sigma_\xi = 20$, $m = 2$; $\sigma_y/\bar{Y}$ is fixed at 0.2.

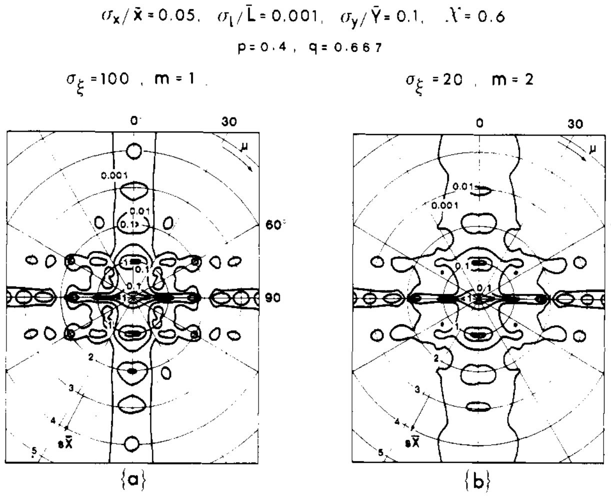

**Figure 17.** SAXS patterns calculated by using the same parameters that were used in Figures 14 and 15 at $\chi = 0.6$: pattern a, $\sigma_\xi = 100$, $m = 1$; pattern b, $\sigma_\xi = 20$, $m = 1$.

In order to obtain the best fit between the curve observed for the annealed speciment shown in Figure 3 and the calculated curve at $\chi = 0.6$, the parameter $\sigma_y/\bar{Y}$ was set equal to 0.2. Figure 16 shows the results for the parameter sets $\sigma_\xi = 100$, $m = 1$ and $\sigma_\xi = 20$, $m = 2$. It is seen that for $2 \leq s\bar{X} \leq 5$, the peak intensities are weaker than those in Figures 14 and 15 for $\chi = 0.6$. Furthermore, higher order maxima at $s\bar{X} > 5$ are smeared out completely in Figure 16, and when the two curves in Figure 16 are compared, it is seen that a change in the orientational fluctuation of the lamellae does not produce any significant change in the profiles. These calculated curves are in good agreement with the curve observed for the specimen annealed for 45 s, taking into consideration the instrumental broadening.

We now discuss the azimuthal angle ($\mu$) dependence of the scattered intensity distribution calculated by using the same values of the parameters listed in Figures 14–16 for the case of $\chi = 0.6$. Figure 17 shows the results obtained by using the same parameters listed in Figures 14 and 15, in which patterns a and b are calculated with $\sigma_\xi = 100$, $m = 1$ and $\sigma_\xi = 20$, $m = 2$, respectively. In the meridional

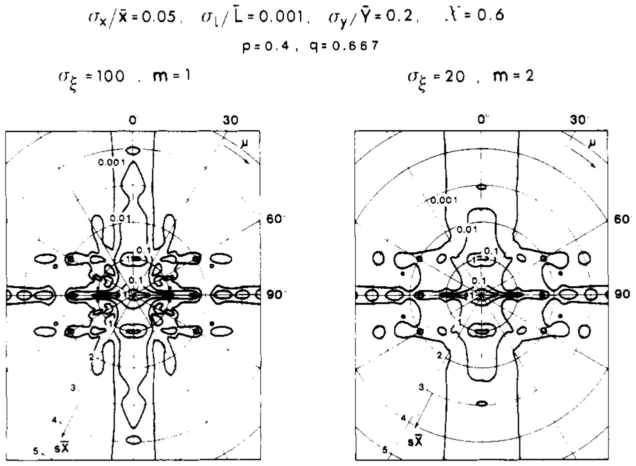

(a) (b)

**Figure 18.** SAXS patterns calculated by using the same parameters that were used in Figure 16: pattern a, $\sigma_\xi = 100$, $m = 1$; pattern b, $\sigma_\xi = 20$, $m = 2$.

direction, an increase of the orientational fluctuation causes the disappearance of the fourth-order intensity maximum and an increase of the $\mu$ dependence of the intensity distribution. Thus Figure 17a is in better agreement with the intensity distribution observed for the unannealed sample than Figure 17b. When $\mu = 90°$, there is considerable disagreement between the observed (Figure 1) and calculated patterns. Many scattering maxima appear in the horizontal direction of the calculated pattern that are not present in the observed pattern. In order to seek the origin of this discrepancy, we consider the behavior of $G_y^2$ at $\mu = 90°$. For mathematical convenience, the treatment was restricted to $\xi = 0°$ and $t = 0$. This system denotes perfect orientation of the lamellae perpendicular to the $X_3$ axis, which is similar to that given by $\sigma_\xi = 100$ and $m = 1$. Equation 10b can then be rewritten as follows:

$$G_y^2 = \left[ \bar{L}\bar{Y}\rho_0 \frac{\sin\{\pi(\chi/p)s\bar{X}\}}{\pi(\chi/p)s\bar{X}} \times \exp\left\{-\frac{1}{2}\pi^2(\sigma_l/\bar{L})^2(\chi/p)^2(s\bar{X})^2\right\}\right]^2 \tag{20}$$

The term $\sin^2\{\pi(\chi/p)s\bar{X}\}$ is a periodic function with maxima occurring at positions defined by

$$\pi(\chi/p)s\bar{X} = (2n-1)\pi/2 \qquad (n = \text{integer}) \tag{21a}$$

which can be rewritten as

$$\bar{L}/\bar{X} = \frac{2n-1}{2} \Big/ (s\bar{X}) \tag{21b}$$

Equation 21b shows that $\bar{L}/\bar{X}$ increases as $n$ increases and $s\bar{X}$ decreases. This indicates that when $\bar{L}$ is sufficiently greater than $\bar{X}$, higher order scattering maxima are shifted to lower scattering angles. Therefore, for the unannealed specimens, which do not show any equatorial maxima, it can be presumed that the average length $\bar{L}$ of the crystal lamellae is much greater than the average long period $\bar{X}$. It follows that the degree of orientational fluctuation of the crystal lamellae must be very small in order to avoid overlapping.

Considering now the comparison between calculated and observed patterns for the annealed samples, we show in Figure 18 the patterns calculated by using the same parameters listed in Figure 16; patterns a and b are calculated for $\sigma_\xi = 100$, $m = 1$ and $\sigma_\xi = 20$, $m = 2$, respectively. In both patterns the second- and third-order meridional maxima become indistinct, in good agreement with the observed pattern. Figure 18b is better than Figure 18a with regard to the annealed sample, taking into consideration the number of the meridional scattering maxima and the fact that the orientational fluctuation may be increased by annealing. By contrast, there is considerable disagreement between the calculated and observed (see Figure 2) equatorial patterns (i.e., when $\mu = 90°$), and this can be rationalized in the same way as discussed above. In comparison with the calculated patterns (Figures 17 and 18), the observed scattering patterns (Figures 1 and 2) exhibit a somewhat larger $\mu$ dependence of the intensity distribution for the scattering maxima in the meridional direction. A greater $\mu$ dependence of the calculated scattering patterns could presumably be realized by introducing an appropriate orientational fluctuation of the "assembly" of crystal lamellae.

In order to simplify the discussions, we have neglected the effect of the thickness of the transition region ($t$) in the present paper. According to the results reported by Blundell,[15] Hashimoto,[16] and Crist,[19] the intensity of the higher order diffraction peaks decreased rapidly as $t$ increased, but the profile of the scattering curve was almost independent of $t$ at lower angles.

## Conclusions

Theoretical calculations of the SAXS intensity distribution for the present system allow the following quantitative conclusions to be drawn.

(1) The orientational fluctuation of the lamellae is less significant in affecting the intensity than the fluctuations of the lamellar thickness and long period. The average length $\bar{L}$ of the crystal lamellae is much greater than the average long period $\bar{X}$. Therefore efficient packing considerations require that the lamellae be oriented with their large flat faces almost parallel to the film surface. This result makes it possible to explain the ultradrawing of the dry polyethylene gel films as described in our earlier papers.[7,13] The existence of large lamellae (i.e., with large lateral dimensions) permits high drawability due to the large numbers of folded segments that are available for the transformation to a fibrous structure.

(2) The increase of the lamellar thickness fluctuation is the major reason that the scattering maxima become indistinct or disappear during annealing. This fluctuation presumably occurs during the recrystallization process when the polymer chains refold into a longer fold period. The increase of the fluctuation of lamellar crystal thickness by annealing is thought to cause an increase in the entanglement mesh (i.e., interpenetration of chains from neighboring crystals) that effectively transmits the drawing forces. This is important to avoid slippage of the polymer chains during the elongation process. In this way we can understand why annealed samples exhibit higher drawability (30 times) by comparison with that of unannealed samples (20 times).

**Registry No.** Polyethylene, 9002-88-4.

## References and Notes

(1) W. O. Statton, *J. Appl. Phys.*, **32**, 2332 (1961).
(2) W. O. Statton and P. H. Geil, *J. Appl. Polym. Sci.*, **3**, 357 (1960).
(3) E. W. Fisher, *Ann. N.Y. Acad Sci.*, **89**, 620 (1961).
(4) E. W. Fisher and G. F. Schmidt, *Angew. Chem.*, **74**, 551 (1962).
(5) A. Keller and D. C. Bassett, *J. R. Microsc. Soc.*, **79**, 243 (1960).
(6) W. O. Statton, *J. Appl. Phys.*, **38**, 4149 (1967).

(7) M. Matsuo and R. St. J. Manley, *Macromolecules*, **15**, 985 (1982).
(8) P. Smith and P. J. Lemstra, *J. Mater. Sci.*, **15**, 505 (1980).
(9) P. Smith and P. J. Lemstra, *Makromol. Chem.*, **180**, 2983 (1979).
(10) P. Smith and P. J. Lemstra, *Colloid Polym. Sci.*, **258**, 891 (1980).
(11) P. Smith, P. J. Lemstra, and H. C. Booij, *J. Polym. Sci., Polym. Phys. Ed.*, **19**, 877 (1981).
(12) P. Smith, P. J. Lemstra, J. P. L. Pijpers, and A. M. Kiel, *Colloid Polym. Sci.*, **259**, 1070 (1981).
(13) M. Matsuo and R. St. J. Manley, *Macromolecules*, **16**, 1500 (1983).
(14) D. J. Blundell, *Acta Crystallogr., Sect. A*, **26**, 472 (1970).
(15) D. J. Blundell, *Acta Crystallogr., Sect. A*, **26**, 476 (1970).
(16) T. Hashimoto, K. Nagatoshi, A. Todo, H. Hasegawa, and H. Kawai, *Macromolecules*, 7, 364 (1974).
(17) M. Matsuo, C. Sawatari, M. Tsuji, and R. St. J. Manley, *J. Chem. Soc., Faraday Trans. 2*, in press.
(18) D. Ya. Tsvankin, *Polym. Sci. USSR (Engl. Transl.)*, **6**, 2304 (1964).
(19) B. Crist, *J. Polym. Sci., Polym. Phys. Ed.*, **11**, 635 (1973).

# Phase Contrast Imaging of Styrene–Isoprene and Styrene–Butadiene Block Copolymers

**Dale L. Handlin, Jr.,**[†] **and Edwin L. Thomas***

*Department of Polymer Science and Engineering, University of Massachusetts, Amherst, Massachusetts 01003.* *Received November 10, 1982*

ABSTRACT: Phase contrast produced in the electron microscope by defocus techniques has been used to obtain the first *unstained* images of styrene–isoprene and styrene–butadiene diblock and triblock copolymers. Theoretical image calculations based on square-wave and circular cross section one-dimensional models were used to demonstrate the effects of mean inner potential difference, interface width, and microscope optics on resultant images. Experimental phase contrast images of microtomed block copolymers with ordered lamellar, cylindrical, and disordered spherical morphologies were in good agreement with theory and with experimental scattering contrast images (osmium tetraoxide stain). Repeat periods in the ordered morphologies were found to be independent of the microscope parameters as theoretically predicted. Calculations show that the compositional profile across the interface between the polymer phases will not be easily measured from experimental phase contrast images because of the smoothing effect of limited electron beam coherence. The phase contrast technique is, however, sufficient to visualize the phase-separated regions of polymers of quite similar atomic composition and/or density, eliminating the need for chemical modification of one or both of the polymers.

## Introduction

Historically, transmission electron microscopy (TEM) has been the principal technique for determining the morphology of styrene–isoprene (SI) and styrene–butadiene (SB) block copolymers. These copolymers represent the large class of phase-separated copolymers, blends, and graft copolymers whose phases are so similar in chemical composition and density that the phases have only been distinguished by the introduction of highly reactive, selective reagents, such as osmium tetraoxide, which bind to or degrade one phase to provide scattering contrast. Phase[24] contrast, however, is much more sensitive to small differences between the two phases which are reflected in their mean inner potentials, permitting phase contrast imaging utilizing electron microscope transfer theory and making staining unnecessary for many polymer systems.

Petermann and Gleiter[1] found negligible scattering contrast between amorphous regions and nondiffracting crystallites in polyethylene films and were the first to employ *phase contrast* for imaging polymer systems. The mean inner potential difference (the mean inner potential (measured in volts) is analogous to the refractive index in light optical phase contrast microscopy) of 1.03 V between crystalline and amorphous regions in polyethylene provided ample phase contrast in films only 10–30 nm thick (see Table I for a listing of mean inner potentials of common polymers). Polystyrene and polyisoprene show a significantly smaller difference in potential of 0.61 V. The potential difference between polystyrene and polybutadiene ranges from 0.08 V (negligible) for 100% 1,4-*cis*-polybutadiene to 0.76 V for 44% 1,4-*cis*-, 42% 1,4-*trans*-, and 14% 1,2-polybutadiene. Therefore block copolymers of SI and certain SB's should be imagable without staining using phase contrast, although with much lower contrast than for polyethylene.

Table I
Mean Inner Potentials of Common Polymers

| polymer | density, g/cm$^3$ | mean inner potential, V |
|---|---|---|
| polystyrene | 1.05 | 7.08 |
| polyisoprene | 0.904 | 6.47 |
| poly(1-butene) | 0.87 | 6.40 |
| polybutadiene | | |
| 1,2 | 0.90 | 6.35 |
| 1,4 (cis) | 0.895 | 7.13 |
| 44% 1,4 cis, 42% 1,4 trans, 14% 1,2 | 0.895 | 6.32 |
| polyethylene | | |
| crystal | 1.00 | 7.35 |
| amorphous | ~0.86 | 6.32 |

The objective of this paper is to demonstrate that even in the absence of crystallinity, phase-separated copolymers of very similar density and composition can be imaged by phase contrast techniques without resorting to stains, which are often artifact inducing, time-consuming, and hazardous to use. Regular SI and SB block copolymers were chosen as model systems because they phase separate in three well-defined morphologies: lamellar, cylindrical, and spherical. Using the transfer theory of imaging, one can predict the phase contrast images of these morphol-

---

[†] Present address: Westhollow Research Center, Shell Development Co., Houston, TX 77001.

0024-9297/83/2216-1514$01.50/0